

Passive ground-based optical techniques for monitoring the on-orbit ICESat-2 altimeter geolocation and footprint diameter

Lori A. Magruder¹, Kelly Brunt², Thomas Neumann³, Bradley Klotz¹, and Michael Alonzo⁴

¹University of Texas at Austin

²University of Maryland, NASA Goddard Space Flight Center

³NASA Goddard Space Flight Center

⁴University of Texas at Austin

November 26, 2022

Abstract

NASA launched its second Earth observing laser altimeter in 2018 with mission objectives of studying the changes in our climate by monitoring global elevations, particularly in the polar regions. Since the mission is focused on generating accurate elevations and elevation change, the geolocation (or geodetic position) of the measurements are of utmost importance to each of the scientific disciplines supported by these observations. Geolocation validation is required to ensure that the mission is meeting its objectives with the appropriate level of geolocation accuracy. One validation technique uses small optical reflectors placed in a specific pattern along one or more satellite ground-tracks. The optics provide a unique signal back to the satellite that can be used to compare the geolocation of these returns in the data to the known position on the surface. Results of the position comparison indicate the measurement locations are accurate to within 3.5 m with a standard deviation of 1.6 m. They also provide a method for determining a representative footprint diameter using geometric analysis, which resulted in an average value of 10.9 m \pm 2.1 m.

22 Plain Language Summary

23 NASA launched its second Earth observing laser altimeter in 2018 with mission objectives
24 of studying the changes in our climate by monitoring global elevations, particularly in the polar
25 regions. Since the mission is focused on generating accurate elevations and elevation change, the
26 geolocation (or geodetic position) of the measurements are of utmost importance to each of the
27 scientific disciplines supported by these observations. Geolocation validation is required to ensure
28 that the mission is meeting its objectives with the appropriate level of geolocation accuracy. One
29 validation technique uses small optical reflectors placed in a specific pattern along one or more
30 satellite ground-tracks. The optics provide a unique signal back to the satellite that can be used to
31 compare the geolocation of these returns in the data to the known position on the surface. Results
32 of the position comparison indicate the measurement locations are accurate to within 3.5 m with a
33 standard deviation of 1.6 m. They also provide a method for determining a representative footprint
34 diameter using geometric analysis, which resulted in an average value of 10.9 m \pm 2.1 m.

35

36 **Abstract**

37 Corner cube retro-reflectors (CCRs) are passive optical components that were used to
38 independently evaluate the ICESat-2 laser altimeter geolocation and laser footprint diameter.
39 These campaigns were performed in both mid-latitude and polar regions over the first 18 months
40 of the mission. A proven technique using CCRs to evaluate the original ICESat mission was
41 optimized for the ICESat-2 mission and deployed at White Sands Missile Range and along the 88°
42 S line of latitude to passively monitor the geolocation accuracy, and estimate the diameter of the
43 laser footprint. The results reveal an average geolocation accuracy of the ICESat-2 measurements
44 to within 3.5 m \pm 2.1 m, meeting the mission requirement of 6.5 m. Additionally, the CCR
45 evaluation of the footprint diameter resulted in 10.9 m \pm 1.3 m, with the variability explained
46 primarily through the influence of atmospheric conditions.

47 **1. Introduction**

48 The Ice, Cloud and land Elevation Satellite-2 (ICESat-2) is a NASA Earth observing
49 satellite, on-orbit since September 2018. The motivation behind the mission is focused on
50 observations over the polar regions to support ice-sheet elevation change and sea ice
51 characterization studies. The observations are realized through ATLAS (Advanced Topographic
52 Laser Altimeter System), a lidar instrument designed to provide precise ranging measurements of
53 individual, 532 nm laser photon reflections from the surface of the Earth. These ranging
54 measurements, combined with the satellite observatory position and laser pointing determination
55 create a capability to quantify centimeter-scale elevation change over the ice sheets and sea ice
56 freeboard (Neumann et al., 2019). ATLAS uses a single laser to provide 6 altimeter beams at 10
57 kHz. The beams are configured into 3 beam pairs with pairs spaced by ~3.3 km across track
58 (Markus et al., 2017). Within each pair the spots are separated in the along-track direction by 2.5
59 km and 90 m in the across-track direction. Additionally, the pairs provide two distinct energy
60 levels with the ‘strong’ spot at 4 times the level of the ‘weak’. The locations of the weak/strong
61 spots in the 6 beam pattern is dependent on the orientation of the observatory relative to the
62 direction of motion.

63 The mission requirements on satellite position and pointing determination ensure that the
64 observations accurately support the mission science objectives with respect to geolocation.

65 Precision orbit determination (POD) is required to be within 5 cm radial accuracy while the
66 precision pointing determination (PPD) requires laser pointing knowledge to within 3.7 μ rad of
67 precision, resulting in a total measurement geolocation knowledge of 6.5 m, or \sim 2.7 arc sec. The
68 PPD solution quality is dependent on the ability to resolve the influence of thermal variations and
69 spacecraft orientation on the pointing efficacy (Luthcke et al., 2019). Pointing corrections on-orbit
70 are determined using a regular sequence of maneuvers over the ocean ('ocean scans') and within
71 a full orbit ('around the world scans') to recover the range residuals and biases (Luthcke, et al.,
72 2005). These calibrations are applied to the PPD to reach the pointing accuracy to support the
73 mission geolocation requirement. Methods for validating the geolocation utilize comparison to
74 ground reference surfaces, derived independently with high resolution airborne lidar (Magruder et
75 al., 2020) or ground based GPS surveys (Brunt et al., 2019) to determine the vertical and horizontal
76 accuracy of the ICESat-2 geodetic position.

77 A unique, independent method for geolocation accuracy assessment relies on small optical
78 components, corner cube retroreflectors (CCRs). CCRs are designed to reflect light along the angle
79 of incidence with diffraction properties dependent on the CCR diameter and energy wavelength
80 (Sun et al., 2019). As such, careful selection of diameter allows the ground-based optics to return
81 observable reflections to a space-based receiver (Magruder et al., 2020). These CCR signatures
82 are distinct from the surface returns at the measurement rate, meaning no post-processing or
83 aggregation is necessary to identify the presence of reflections from the optics within the data.
84 Comparing the satellite measurement geolocation to the known geodetic position of the CCR gives
85 the independent assessment of measurement positional accuracy. This technique was successful
86 for ICESat (2003-2009; Magruder et al., 2005) and the airborne engineering testbed for ICESat-2,
87 MABEL (Multi Altimeter Beam Experimental Lidar; Magruder and Brunt, 2018). Studies with
88 MABEL determined the expected response of a CCR to photon-counting lidar and helped design
89 the specific implementation details. The arrays placed at White Sands Missile Range (WSMR)
90 utilized 8 mm diameter optics on poles with height variations from 0.6 m to 3 m in four arrays
91 (Magruder et al., 2020a). CCR arrays placed along the 88° S (88S) line of latitude during a GNSS
92 ground survey performed in 2017-2018 Antarctic summer season and revisited each year since use
93 CCRs positioned where the satellite reference tracks (RGTs) spatially converge. The WSMR
94 arrays are a diamond pattern with CCR arrays located at each of the vertices (north, south, east,
95 and west). This pattern is capable of capturing a beam pair for both ascending and descending

96 tracks. For example, an ascending track could illuminate the east and north arrays with the right
97 beam of a pair and the south and west array with the left beam of the pair. The design of the full
98 ensemble at each CCR validation assumes the ICESat-2 satellite meets the pointing control
99 requirement of ± 45 m and the ability to maintain RGT tracking (Magruder et al., 2020b).

100 Here we present an evaluation of the ICESat-2 positional (horizontal geolocation) accuracy
101 of the laser footprint and the estimation of the effective footprint diameter using all available CCR
102 signature returns for the current mission lifetime (October 2018 – May 2020). Further, this study
103 explores the variations in the results to radiometric effects due to the state of the atmosphere. The
104 methods presented here provide an opportunity to passively monitor the performance of the
105 satellite on-orbit. This method is critical to the continuous validation of ICESat-2, as it helps ensure
106 that the scientific discoveries leveraging higher-level data products are based on accurate and
107 precise low-level data.

108 **2. Data and Methods**

109 The CCR analysis focuses solely on the ICESat-2 Global Geolocated Photons (ATL03) data
110 product. ATL03 is the Level 2a data product that provides the photon positional data in addition
111 to many other parameters associated with uncertainties, corrections for tides and atmosphere and
112 signal statistics (Neumann et al., 2019a). The ATL03 data used in this study are available through
113 the National Snow and Ice Data Center (www.nsidc.org) and are part of the third release (r003) of
114 final data products from the ICESat-2 Project Science Office (Neumann et al., 2019b). Since
115 ATL03 includes photons associated with both surface reflections and solar background noise, the
116 ATL03 processing algorithm also includes a filtering method that statistically delineates between
117 the two. This is an important step particularly for the majority of the higher, Level 3a, products
118 that rely on those photons identified with a high surface-signal probability to interpret the surface
119 elevation (Smith et al., 2019, Kwok et al., 2019, Neuenschwander and Pitts, 2019).

120
121 The ICESat-2 reference ground-tracks (RGTs) create several opportunities to point ATLAS at the
122 WSMR validation site using the up to 5 degree off-nadir pointing capability of the observatory.
123 These 7 WSMR relevant RGTs equate to opportunities nearly twice a month over the course of
124 the repeat ground-track cycle (91 days) and offer scenarios for both ascending and descending
125 tracks. This variability in satellite direction of motion (northward or southward), combine with

126 possible orientation (forward or backward facing) and solar panel position to provide a
127 comprehensive method for understanding the efficacy of the pointing calibration, the pointing
128 control and overall geolocation knowledge of the satellite-based measurements under on-orbit
129 conditions specific to a mid-latitude orbital position.

130

131 The CCR arrays deployed along the 88S line of latitude during a GPS traverse in the 2017-
132 2018 Antarctic field season (Brunt et al., 2019) and resurveyed or relocated during the following
133 two field seasons to optimize the opportunities for CCR illumination based on the results from the
134 previous year. Given the 92° orbit inclination, the ground tracks spatially converge at the extreme
135 latitudes and provide a dense coverage of the region, allowing for many more CCR potential
136 overpass opportunities than the WSMR location.

137

138 The analysis of the CCR signatures is described in Magruder et al. (2020a) and initiates with
139 finding the elevated, linear signatures distinct from the estimated terrain surface in the relevant
140 ATL03 transects. The second processing step extracts the CCR returns and generates a statistical
141 estimate of along-track signal CCR length using the expected Gaussian energy distribution of the
142 laser footprint. The laser footprint diameter is representative of a Gaussian beam diameter, as
143 defined as the 2-sigma value of the signal distribution curve representative of 86% of the total
144 beam energy based on pre-launch measurements of a Gaussian energy pattern (Martino et al.,
145 2019). For a strong beam, the Gaussian beam energy value is $120 \mu\text{J}$ while a weak beam provides
146 $30 \mu\text{J}$ (Neumann et al., 2019a). The CCR returns are quite pronounced but it is estimated that the
147 spatial extent of the footprint size is susceptible to atmosphere attenuation or other optical losses.
148 In this paper, we use the same statistically robust methodology of Magruder et al. (2020a) on the
149 much larger set of CCR returns collected since that initial study. The chord length (e.g. the
150 effective distance from leading edge to trailing edge of the initial illuminating footprint and final
151 illuminating footprint respectively) is critical to understanding where the CCR is located relative
152 to the center of the laser footprint diameter. Based on the ATL03 geolocation algorithm, the
153 specific position of a reflector within the footprint diameter is unresolvable as the geolocation for
154 all of the surface-reflected photons for a given shot are geolocated to the laser footprint centroid
155 (Luthcke et al., 2019). The CCR deterministic position within a laser footprint relies solely on its
156 relative position to the footprint centerline that can be quantified by the length of the signal chord

157 length. This is more of an estimation when only one CCR is illuminated and the scenario lacks the
158 geometric constraint for determining which side (east or west) of the footprint centerline the CCR
159 is located. However, when two or more CCR signatures appear in a single transect, both the ATL03
160 geolocation accuracy and the Gaussian beam diameter can be determined. These estimations are
161 derived using the known geometry of the CCR positions and the goodness of fit of the CCR signal
162 signatures for a given beam diameter through an iterative process. By minimizing the horizontal
163 residuals of the combined comparison over the sequence of CCR illuminations a quantitative
164 assessment is achieved for the geolocation offsets in northing and easting that inform the accuracy
165 of the horizontal position of the measurements.

166

167 Determination of geolocation accuracy and footprint diameter is dependent on the signal
168 retrieval. Adequate signal retrieval implies that there is reasonable number of signal photons for
169 accurate analysis given the retrieval technique. The number of signal photons depend on both the
170 incident energy at the surface and returned energy at the receiver. The signal reflection strength is
171 primarily dependent on the surface reflectance. However, atmospheric attenuation also is
172 significant. Clouds, aerosols and water vapor in the atmospheric column attenuate the laser light
173 through absorption and scattering. Initial predictions based on data prior to ICESat-2 launch
174 suggested that column optical depth, a measure of the observed attenuation related to clouds and
175 aerosols, could attenuate $> 50\%$ of the laser energy if the optical depth is above 1.0 (Palm et al.
176 2020).

177

178 To assess the atmospheric effects on the CCR geolocation validation and diameter retrievals,
179 calibrated attenuated backscatter (CAB) and lower along-track-resolution parameters, including
180 relative humidity, temperature, and pressure, are utilized from the ICESat-2 atmospheric product
181 ATL09 (Palm et al., 2019). Specific humidity is determined from these variables following the
182 computation of vapor pressure through the standard equations provided in Rogers and Yau (1996).
183 The atmospheric profiles are separated into estimated boundary layer (surface – 1 km), low (1 km
184 – 5 km), moderate (5 – 10 km), and high altitudes (10 – 15 km) to pinpoint specific levels where
185 the moisture content is potentially high or where temperature inversions may trap scattering
186 particles. For the cases at WSMR, the column optical depth and profile data are used to assess their
187 effect on footprint diameter and associated geolocation accuracy. For those cases examined at 88S,

188 other parameters are considered from the atmosphere product, including the blowing snow
189 confidence level which could cause additional attenuation through signal scattering. Moisture
190 effects on the signal retrieval are more likely at WSMR than at 88S because temperatures are
191 higher and the air can hold more water vapor. The depth of the troposphere at the mid-latitudes
192 extends above 12 km height as well, especially during the summer months. For comparison, the
193 tropospheric depth at 88S extends only to ~8 km before noticeable stratospheric warming begins.
194 Therefore, the impact of the atmosphere will be different for the two locations based on these
195 differences in atmospheric column characteristics.

196 **3. On-orbit assessment 2019-2020**

197 The first successful WSMR overpass in March 2019 captured the center weak beam on
198 both the east and the north arrays. This initial analysis helped assess the geolocation of the ATL03
199 photons relative to the CCR positions for the first time and also helped establish the deterministic
200 method for recovery of the footprint diameter (Magruder et al., 2020a). The result for this particular
201 pass was a footprint diameter of 10.6 m and the ATL03 horizontal geolocation was accurate to
202 within 2 m. This was an important discovery for several reasons that include: 1) the automation of
203 the footprint diameter determination which proved to significantly impact the ability to retrieve
204 the correct position of the CCR within the spatial extent of the illuminated areas; and 2) the
205 realization of how the spacecraft pointing is implemented and executed in addition to
206 understanding the constraints on the spacecraft pointing stability.

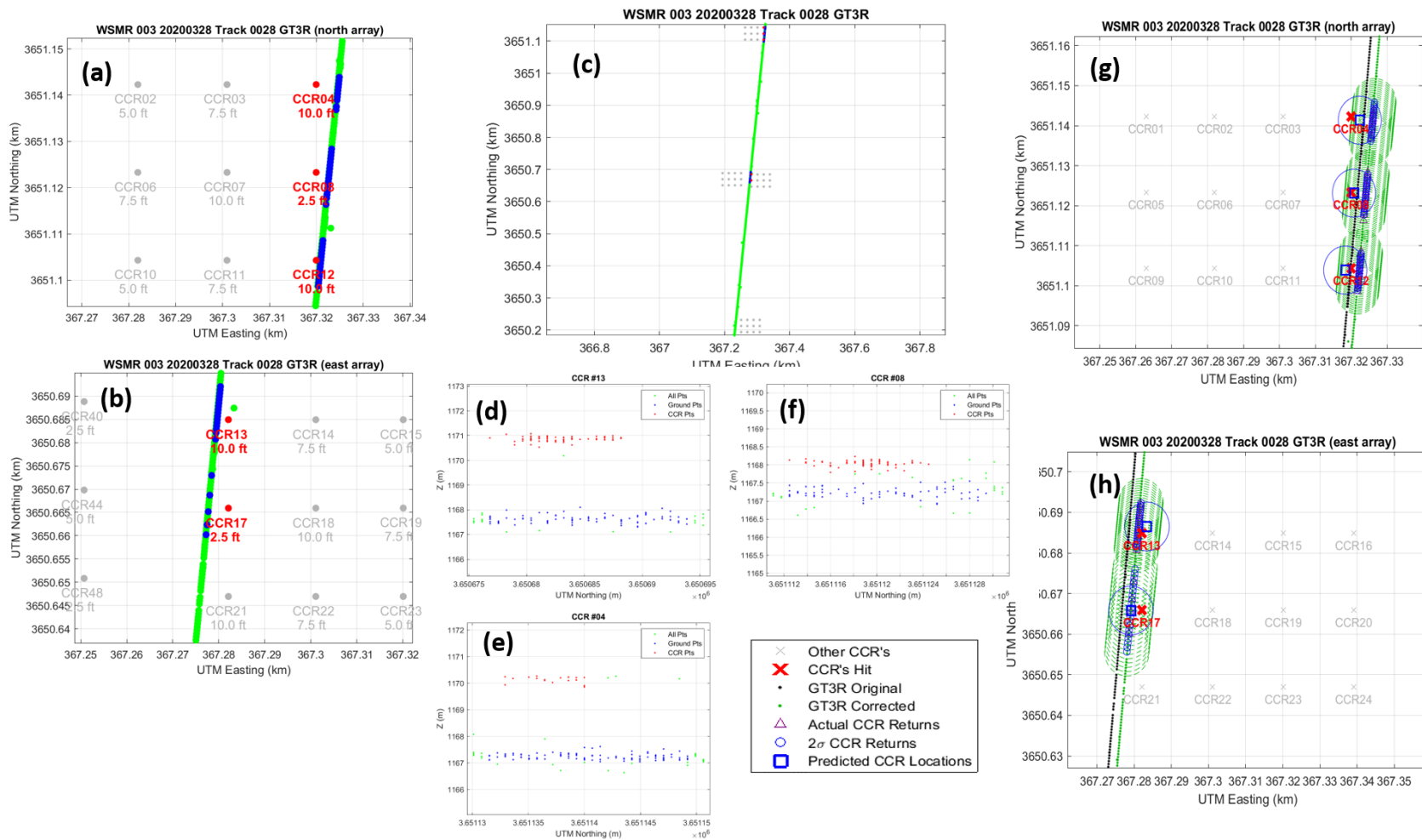
207

208 Favorable conditions in September 2019 allowed for the illumination of multiple CCRs
209 with the center strong beam, during the second opportunity to explore the validation technique.
210 The analysis of these signatures indicates a beam diameter of 12 m and horizontal geolocation
211 offset of 5 m. The disparity in diameter recovered between the weak (March 2019) and strong
212 (September 2019) beams, at the time, was attributed to atmosphere attenuation and potential loss
213 of return signal at the edges of the footprint where the energy is lower (Magruder et al., 2020).
214 Given the two instances of CCR signal retrievals, the concept and implementation were confirmed
215 but the small sample size of data did not warrant statistically relevant conclusions for geolocation
216 accuracy and beam diameter. As such, the pointing requests continued with regularity for the
217 relevant RGTs within each full 91-day orbit cycle. Varied results were achieved at WSMR as some
218 unsuccessful overpasses simply did not hit the CCR arrays while others were performed during

219 cloud cover that prevented returns from either the surface or the CCR. Other opportunities occurred
220 coincident to anomalous satellite operational events which temporarily suspended on-orbit data
221 collection. RGT #28, a descending pass on 28 March 2020 was particularly successful by
222 illuminating 5 CCRs in both the north and east arrays after the satellite performed a roll maneuver
223 to point $\sim 4^\circ$ off-nadir. Figure 1 (a – c) provides the configuration of the satellite ground track
224 (ATL03 geolocated photons) and the array locations. In Figure 1 the signal photons attributed to
225 the CCR returns are blue and the remaining ATL03 signal photons are green. Figure 1 (d-f)
226 presents the along-track segments for three different CCRs that were illuminated. The heights of
227 the individual signatures provide the initial identification of a specific CCR, as they were deployed
228 with staggered heights with this consideration. In this case of Figure 1 (d-f), the sequential heights
229 of 3 m, 0.75 m and 3 m, from North to South, is indicative of a CCR04, CCR08 and CCR12
230 illumination pattern. The identification of the CCRs in the east array is done similarly (CCR13 and
231 CCR17). The signature chord length of each of the CCRs is statistically derived using a 2σ value
232 from a Gaussian distribution of the extracted CCR signal. Using these chord lengths with the
233 geometric constraints from the known CCR array positions results in a 12.0 m beam diameter and
234 a horizontal geolocation offset of 4.3 meters (RMSE 2.1 m). The RMSE is representative of the
235 goodness of fit of the predicted geolocation track to the 5 individual CCR positions. Figure 1 (g-
236 h) illustrates the geolocation adjustment of the original track (black line) to accommodate the
237 geometry of the known CCR locations (red X's) and the signal chord lengths (blue points) as an
238 indicator of where the CCR is relative to the centerline of the laser footprint. The solution of the
239 true positions (green points) allows the technique to estimate the accuracy of the ATL03
240 geolocation.

241

242



243

244 Figure 1. Signal analysis for WSMR overpass on 28 March 2020 where the laser illuminated 5 CCRs within one descending ground track; 3 of the illuminated
 245 CCRs were in the north array and 2 were in the east. Plots (a-c) show the ATL03 surface signal in green and the ATL03 CCR signal in blue. Plots (d-f) provide the
 246 returns from CCR04, 08 and 12 in the north array indicating the height of each CCR relative to the surface. Plots (g-h) show the estimated chord lengths (blue) and
 247 the solution (green) for determination of the footprint diameter and geolocation offsets that correspond to the geometry of the known locations of the illuminated
 248 optical components.

249

WSMR overpass date	Beam Ground-track	Beam strength	Off-nadir angle (deg)	Slant range (m)	ATLAS spot number	Local time of collection	Horizontal geolocation error (m)	Footprint diameter (m)
3/31/2019	GT2R	Weak	2.46	485162	4	08:37	2.5	10.6
5/31/2019	GT2R	Weak	0.37	484743	4	17:04	3.0	8.5
9/28/2019	GT2R	Strong	2.52	485037	3	11:56	5.0	12.0
10/12/2019	GT2R	Strong	4.87	486609	3	23:15	3.8	10.6
10/31/2019	GT2R	Strong	3.27	484847	3	10:24	2.8	11.4
1/07/2020	GT1R	Strong	3.22	485483	5	18:03	0.7	8.3
2/08/2020	GT3R	Strong	1.67	484471	1	16:31	7.7	11.6
3/28/2020	GT3R	Strong	4.06	485998	1	03:16	4.3	12.0
5/09/2020	GT3R	Strong	1.72	484482	1	13:11	2.1	10.0
Average WSMR geolocation error and beam diameter							3.5 ± 1.9	10.6 ± 1.3
88S overpass date	Beam Ground-track	Beam strength	Off-nadir angle (deg)	Slant range (m)	ATLAS spot number	Local time of collection	Horizontal geolocation error (m)	Footprint diameter (m)
12/10/2018	GT2R	Strong	-	511475	3	21:49	0.4	11.6
1/18/2019	GT3L	Strong	-	511930	5	19:17	2.4	9.8
11/27/2019	GT3L	Weak	2.78	512538	2	04:27	3.3	11.1
12/30/2019	GT3R	Strong	2.81	512031	1	02:55	2.0	12.4
1/13/2020	GT2R	Strong	0.67	511625	3	04:47	8.5	11.5
1/24/2020	GT3R	Strong	2.81	512554	1	22:31	3.8	11.5
Average 88S geolocation error and beam diameter							3.4 ± 2.5	11.3 ± 0.8

250

251 4. Discussion

252 The overpass summary for on-orbit performance of ICESat-2 serves as evidence of the
253 mission meeting both the requirement for geolocation accuracy and the pointing control capability.
254 Table 1 provides the results of each relevant case at WSMR and 88S. Aggregation of the results
255 give an average footprint diameter of 10.9 m with a standard deviation of 1.2 m and a median value
256 of 11.4 m. The horizontal geolocation error, overall, is $3.5 \text{ m} \pm 2.1 \text{ m}$. Results specific to WSMR
257 indicate the diameter retrievals are fairly consistent over the 9 cases within a range of 8.3 m to 12
258 m (average value $10.6 \text{ m} \pm 1.3 \text{ m}$). Using the 6 overpass cases for 88S independent of WSMR
259 determines an average diameter of $11.3 \text{ m} \pm 0.8 \text{ m}$. The pre-launch measurements of the ATLAS
260 laser beam divergence were $21.4 \text{ } \mu\text{rad}$ and $19.7 \text{ } \mu\text{rad}$ for the semi-major and semi-minor axes
261 respectively (A. Martino, pers, comm.). Using these pre-launch measurements and the orbital
262 altitude range of ICESat-2 (486 km – 512 km) yields 9.5 m/10.4 m – 10.0 m/10.9 m for the semi-
263 major and semi-minor axes of the laser spots on the surface, in good agreement with our
264 observations.

265 To understand more completely the variability in footprint diameter retrievals we evaluated
266 parameters that might influence the footprint characteristics at the surface. Figure 2 provides a
267 summary of the correlation or lack of correlation between the footprint diameter values and these
268 parameters investigated and is discussed in the subsequent sections.

269 4.1 Satellite Altitude

270 Since the ICESat-2 orbit is nearly frozen, the satellite altitude has a dependence on latitude.
271 Although the altitude at WSMR for each overpass are $\sim 484 \text{ km}$, the slant range associated with the
272 off-nadir pointing angle (Table 1) creates a longer divergence path length. However, the largest
273 off pointing angle theoretically increases the spot size by only 5 cm relative to the nadir. The
274 average altitude at 88S is nearly 30 km higher than at WSMR which would implies that the spot
275 would be larger by $\sim 1 \text{ m}$ if solely based on path length. The 0.7 m average diameter difference
276 between the two sites' altitudes is consistent with this expected variation but does not account the
277 potential impact of diameter retrieval relative to along-track alignments with the major or minor
278 axes. The lower variability in diameter values at 88S in comparison to that at WSMR could be
279 attributed to the consistency of the collection parameters (altitude and path length) or the lower
280 susceptibility to atmospheric influence based on the reduced vertical height of the boundary layers

281 and the low water vapor content in this region. The relationship between the diameter retrievals
282 and slant range is provided in Figure 2(d) for all cases.

283 4.2 Atmospheric Parameters

284 The atmospheric parameters examined are based on the GEOS-FPIT model results used to
285 calculate the wet and dry tropospheric correction to ATL03 photon heights (Palm et al., 2019).
286 Figure 2(a-c) shows column properties comparison for two specific cases at WSMR, while Figure
287 2(e-f) make similar column-property comparisons between all of the passes at both WSMR and
288 88S.

289 *Humidity.* The relative humidity (RH) and specific humidity (SH) profiles for WSMR in
290 Figures 2(a-b) indicate large amounts of moisture in the lower atmosphere for the 31 May 2019
291 (8.5 m diameter) case, where SH is > 2 times larger than for the 28 March 2020 (12.0 m diameter)
292 case at 4 km above the surface. Overall, at WSMR, the decrease in diameter with increasing SH
293 confirms that moisture content has a negative effect on detecting surface signal. Footprint
294 diameters for WSMR and 88S are shown with respect to the total SH and RH in Figure 2(f). RH
295 and SH are used here to indicate the amount of water vapor present in the lowest portion of the
296 atmosphere. Figure 2(f) indicates that RH is high throughout the column, but these results are
297 misleading due to the cold temperatures at 88S, which are < -23 °C near the surface for all cases.
298 The average temperature at WSMR near the surface was 13.4 °C. Because of this 36 °C difference,
299 the 88S specific humidity is an order of magnitude lower than at WSMR. Overall, SH for the cases
300 at 88S are nearly the same across each instance regardless of apparent footprint diameter
301 determined with the CCR method and thus do not indicate moisture is having an effect on surface
302 signal at this location.

303 *Optical Depth.* The column optical depth comparison for the May 2019/March 2020 results
304 at WSMR in Figure 2(c) indicates a correlation between increasing optical depth and smaller
305 diameters due to increasing attenuation. Initially, the column optical depth was analyzed to
306 determine the presence of cloud and aerosol layers as the most probable parameter for indicating
307 signal attenuation. However, the ATL09 CAB and related parameters capture only limited
308 information on the state of the atmosphere at a given location. Clouds above the 12 km threshold
309 are typically not detected and increased moisture in the lower atmosphere is also not well detected.
310 With increased moisture content, the possibility of additional aerosols not observed by the satellite

311 increases as well. Looking over all WSMR cases in Table I, Figure 2(e) indicates that the primary
312 range of optical depths is between 0.05 – 1.05, although there are several cases that exceed 1.05.
313 It is fitting that the cases with the largest diameters have the lowest optical depths, but there is not
314 a clear statistical relationship determined. For the 88S CCRs, the column optical depth is high for
315 the lowest diameter case but remains low to moderate for the other cases. There is potential for
316 optical depth to be useful at 88S due to a lower tropospheric height (i.e., below the ICESat-2
317 threshold) and lack of water vapor in the atmosphere, but there is no apparent trend within this
318 small sample.

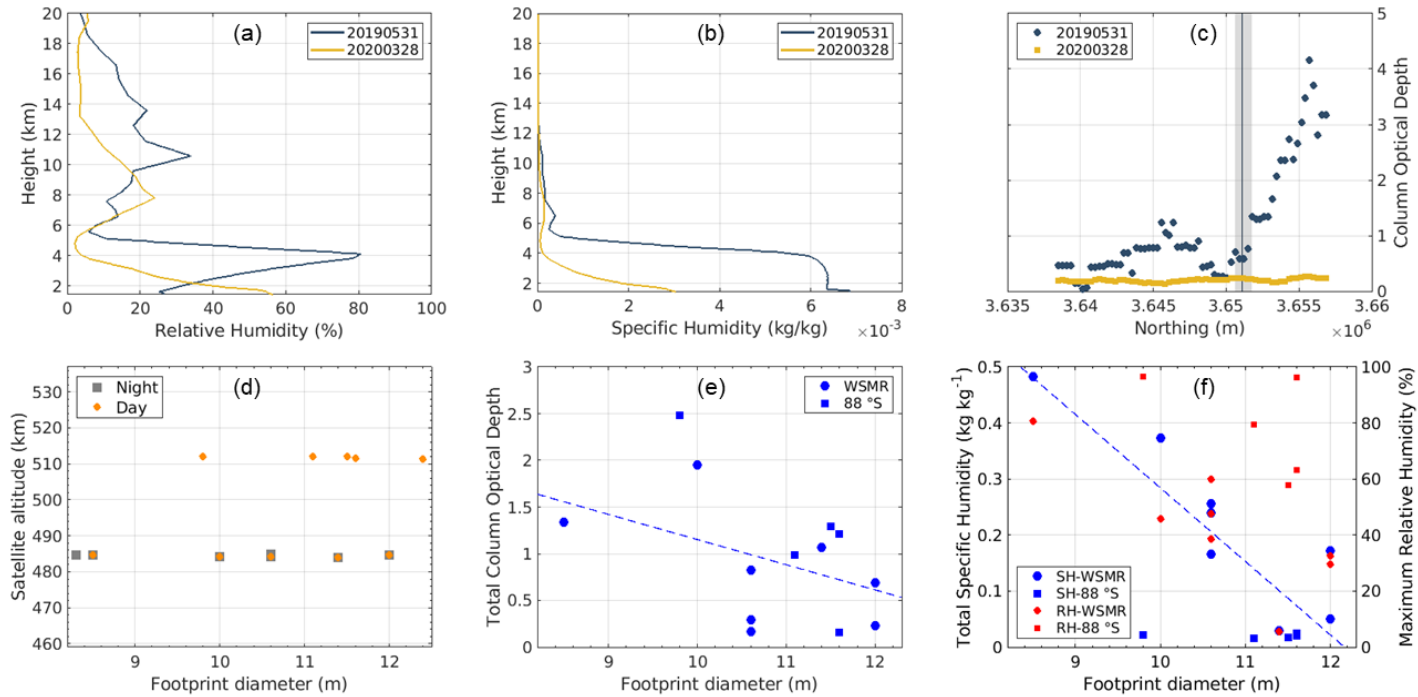
319 *Atmospheric Parameter Summary.* The trends described, although based on an overall
320 small amount of data, suggest that moisture content is inversely related to the footprint diameter
321 for mid-latitude locations, where the moisture content values are more significant than in the polar
322 regions. Increased moisture could indicate that there is also an increase in forward scattering that
323 widens the full laser footprint at the surface but lowers the detected energy, relative to clear
324 atmosphere. That is, the scattering creates a higher probability that the signal photons on the outer
325 edges of a widened footprint are mistaken for noise or are further scattered. While the connection
326 with atmospheric moisture content at 88S is not apparent, another potential cause of low-level
327 attenuation at 88S is blowing snow in the near-surface layer. Blowing snow acts similarly to an
328 aerosol layer, where the small ice crystals provide both forward scattering and backscattering on
329 the laser energy. Although not shown, the case with the lowest diameter had a moderate blowing
330 snow identified in ATL09, but several of the other ‘normal’ diameter cases also had at least
331 moderate blowing snow detected. Additional data collection in the coming Austral summer might
332 help with a more in depth understanding of the relationship between ICESat-2 footprint diameters
333 and both blowing snow and optical depth.

334

335 4.3 Seasonality of Returns from 88S

336 We note that we only received returns from the Antarctic CCRs during the austral summer
337 months (late November through late January) despite nominal pointing control throughout the
338 calendar year. While it is possible that individual attempts at pointing to a CCR array could be
339 compromised by blowing snow or a snowfall event that attenuates the laser returns, this seems like
340 an unlikely explanation for the total lack of CCR returns over the Feb – November months. We

341 note that the surface reflections during this time period were nominal (Brunt et al., 2019)and
342 suggest that the lack of CCR returns in the Austral winter is due to frost build up on either the
343 optical glass or the plastic cap that holds the optical glass due to near-surface atmospheric
344 supersaturation. This could be tested by relative humidity measurements at the CCR sites, or
345 mitigated by heating the CCRs during satellite overpasses, but we acknowledge the difficulty of
346 making humidity measurements at such low ambient temperatures. CCR signatures are recovered
347 shortly after the sun rises at this latitude, suggesting a thermodynamic explanation.



348

349 Figure 2. Comparisons of relative humidity (RH) profiles, specific humidity (SH) profiles, and column optical depth are provided in (a), (b), and (c), respectively,
 350 for the 31 May 2019 (8.5 m diameter) and 28 March 2020 (12.0 m diameter) WSMR cases. The line and gray shading in (c) mark the location of the CCRs. In (d),
 351 footprint diameter is evaluated with the satellite altitude for WSMR and 88S. Day and night designation is provided as well. Panel (e) show the column optical
 352 depth and panel (f) shows the total SH and maximum RH in the lower atmosphere with respect to footprint diameter for WSMR (blue circles) and 88S (blue
 353 squares). The dashed line in (f) is the best-fit for WSMR cases only.

354 **6. Summary**

355 We have shown that the passive method of CCR signature analysis provides an assessing
 356 and monitoring capability for geolocation validation of space-based laser altimetry. The results
 357 from two validation sites indicate that ICESat-2 geolocated photons are accurate to within the
 358 mission requirement of 6.5 m. The methodology also provides an assessment of the effect laser
 359 spot diameter. To date, the successful satellite overpasses of the sites conclude that the diameter
 360 of the ATLAS footprint is 10.9 m \pm 1.3 m. The variation in independent diameter value retrievals
 361 is associated with spacecraft altitude, atmospheric attenuation that can be correlated to optical
 362 depth and humidity, or moisture levels.

363 **Acknowledgments and Data Availability**

364 The authors wish to thank the ICESat-2 Project Science Office for the support under NASA
 365 grant NNX15AC68G. We thank the three 88S Traverse teams, the NSF Office of Polar Programs,
 366 and the numerous personnel with the U.S. Antarctic Program for supporting the deployment of the
 367 Antarctic CCR arrays. Special thanks to colleagues at the Antarctic Meteorological Research
 368 Center for discussions on the potential for CCR frost build up. Data used in this study is compliant
 369 with FAIR data standards and publically available/archived at National Snow and Ice Data Center:
 370 doi: <https://doi.org/10.5067/ATLAS/ATL03.003>

371 **References**

- 372 Brunt, K. M., Neumann, T. A. and Smith, B. E. (2019), Assessment of ICESat-2 ice-sheet surface
 373 heights, based on comparisons over the interior of the Antarctic ice sheet. *Geophysical*
 374 *Research Letters*, 46(22), 13,072-13,078, doi:10.1029/2019GL084886.
- 375 Luthcke, S.B, Pennington, T., Rebold, T., and Thomas, T. (2019), Algorithm Theoretical Basis
 376 Document (ATBD) for ATL03g ICESat-2 Receive Photon Geolocation, ICESat-2
 377 Scientific Computing Facility, [https://icesat-](https://icesat-2.gsfc.nasa.gov/sites/default/files/page_files/ICESat2_ATL03g_ATBD_r002.pdf)
 378 [2.gsfc.nasa.gov/sites/default/files/page_files/ICESat2_ATL03g_ATBD_r002.pdf](https://icesat-2.gsfc.nasa.gov/sites/default/files/page_files/ICESat2_ATL03g_ATBD_r002.pdf)
- 379 Magruder, L. A., and K. M. Brunt (2018), Performance analysis of airborne photon-counting lidar
 380 data in preparation for the ICESat-2 mission, *IEEE Trans. Geosci. and Rem. Sensing*, 56,
 381 2911-2918, doi: 10.1109/TGRS.2017.2786659.
- 382 Magruder, L., K. Brunt and M. Alonzo (2020a), Horizontal geolocation validation for ICESat-2
 383 with corner-cube retroreflectors, *Remote Sensing*, in revision.
- 384 Magruder, L., T. Neumann and N. Kurtz (2020b), Overview of the ICESat-2 mission, *Geophysical*
 385 *Research Letters*, in review.

- 386 Markus, T., and Coauthors (2017), The Ice, Cloud, and land Elevation Satellite-2 (ICESat-2):
387 Science requirements, concept, and implementation, *Rem. Sens. of Env.*, 190, 260-273,
388 doi: 10.1016/j.rse.2016.12.029.
- 389 Martino, A.J., Neumann, T.A., Kurtz, N.T. and McLennan, D. (2019) ICESat-2 mission overview
390 and early performance, *Proc. SPIE 11151, Sensors, Systems and Next-Generation*
391 *Satellites XXIII*, 111510C; <https://doi.org/10.1117/12534938>.
- 392 Neuenschwander, A., and K. Pitts (2019), The ATL08 land and vegetation product for the ICESat-
393 2 mission, *Rem. Sens. of Env.*, 221, 247-259, doi: 10.1016/j.rse.2018.11.005.
- 394 Neumann, T.A., and Co-Authors (2019a), The Ice, Cloud and Land Elevation Satellite-2 mission:
395 A global geolocated photon product derived from the Advanced Topographic Laser
396 Altimeter System, *Remote Sens. Of Env.*, 233, doi: 10.106/j.rse.2019.111325.
- 397 Neumann, T. A., A. Brenner, D. Hancock, J. Robbins, J. Saba, K. Harbeck, A. Gibbons, J. Lee, S.
398 B. Luthcke, T. Rebold, et al. (2019b). *ATLAS/ICESat-2 L2A Global Geolocated Photon*
399 *Data, Version 3*. Boulder, Colorado USA. NASA National Snow and Ice Data Center
400 Distributed Active Archive Center. doi: <https://doi.org/10.5067/ATLAS/ATL03.003>.
401 [May 2020]
- 402 Palm, S., Yang, Y., & Herzfeld, U. (2020). Algorithm Theoretical Basis Document (ATBD) for
403 the atmosphere, Part I: Level 2 and 3 data products. ICESat-2 Data Products, [https://icesat-](https://icesat-2.gsfc.nasa.gov/science/data-products)
404 [2.gsfc.nasa.gov/science/data-products](https://icesat-2.gsfc.nasa.gov/science/data-products).
- 405 Rogers, R. R., and M. K. Yau (1996), *A Short Course in Cloud Physics*. Butterworth-Heinemann
406 publishers, pp. 304.
- 407 Smith, B. (2018), Algorithm Theoretical Basis Document (ATBD) for land ice along-track height
408 product (ATL06), ICESat-2 Scientific Computing Facility, [https://icesat-2-](https://icesat-2-scf.gsfc.nasa.gov/atbd_docs)
409 [scf.gsfc.nasa.gov/atbd_docs](https://icesat-2-scf.gsfc.nasa.gov/atbd_docs).
- 410 Schutz, B. E., H. J. Zwally, C. A. Shuman, D. Hancock, and J. P. DiMarzio (2005), Overview of
411 the ICESat mission, *Geophys. Res. Lett.*, 32, L21S01, doi: 10.1029/2005GL024009.
- 412 Sun, X., Smith, D.E., Hoffman, E.D., Wake, S.W., Cremons, D.R., Mazarico, E., Lauenstein, J.,
413 Zuber, M.T., and Aaron, E.C. (2019) Small and lightweight laser retro-reflector arrays for
414 lunar landers, *Applied Optics*, Vol. 58, No. 33, doi: 10.1364/AO.58.009259
415
416